

1. Results

1.1. Virtual Prototyping of Cell Signals

During the course of this thesis, numerical simulations for the microchannel have been carried out. On the one side, a simulation about the shape of a giant magneto resistance (GMR)-sensor signal of cells was performed, where the magnetic momentum was conveyed through magnetic nanoparticles (MNPs) bound to their surface. On the other side, cell aggregates have been looked at in the same manner with different angles respective to the sensor. Both simulations were then correlated to a reference dipole, with the equivalent magnetic momentum distributed in the center of mass.

Additionally, the flow and shear field inside the channel was simulated numerically for the channel cross-section as well as for a particle near the walls. A force equilibrium simulation was also established in a basic manner.

Every simulation was captured in a MATLAB class “MRCyte”, which contains material parameters and constants for all simulations above.

1.1.1. Numerical investigation of immunomagnetic label density and size on quantitative magnetoresistive sensing of single cells and cell aggregates

In order to mimic a immunomagnetically labeled cell flowing over the sensor half bridge, the planar integral of the respective magnetic flux density (\mathbf{B}) was solved analytically. Here, \mathbf{r}_i specifies the distance vector of a single MNP from the sensor plane. The magnetic flux density was converted by the GMR to a resistive change \mathbf{R}_{sig} by scaling it with the GMR-sensitivity S and subsequently into a signal voltage \mathbf{V}_{sig} inside the bridge branch.(Eqs. 1.1 to 1.3)

In the numerical approach, MNPs were randomly sampled on a sphere surface with an equivalent diameter of $4\text{ }\mu\text{m}$ or $8\text{ }\mu\text{m}$. Then, the signal was computed for every MNP during every timestep. Additionally, the MNP distribution was rotated in every iteration to resemble a rolling motion. The computed signals were then cross-correlated to the signal of a reference flux density \mathbf{B}_{ref} caused by a point-like magnetic moment located in the geometric center of the same sphere.

$$\mathbf{B}(t) = \sum_{i=1}^N \frac{1}{A_{\text{Sensor}}} \int_{-\frac{l}{2}}^{\frac{l}{2}} \int_{-\frac{w}{2}}^{\frac{w}{2}} \frac{\mu_0}{4\pi} \left(\frac{3\mathbf{r}_i(t) (\mathbf{r}_i(t) * \mathbf{m}_i)}{|\mathbf{r}_i(t)|^5} - \frac{\mathbf{m}_i}{|\mathbf{r}_i(t)|^3} \right) dx dy \quad 1.1$$

$$\mathbf{R}_{sig}(t) = -\mathbf{B}(t) * \frac{S}{100} * R + R \quad 1.2$$

$$\mathbf{V}_{sig}(t) = \frac{\mathbf{R}_{sig}(t)}{R + \mathbf{R}_{sig}(t)} * V_p - \frac{V_p}{2} \quad 1.3$$

By its formula, cross-correlation $R_{xy}(\tau)$ yields a displacement dependent signal through its convolution of the complex conjugated reference signal $V_{ref}^*(t)$ with the sample signal $\mathbf{V}_{sig}(t + \tau)$. (Eq. 1.4) Therefor, only the maximal correlation of this function was considered in further analyses.

$$\max\{R_{xy}(\tau)\} = \max \left\{ \int_{-\infty}^{\infty} V_{ref}^*(t) \mathbf{V}_{sig}(t + \tau) dt \right\} \quad 1.4$$

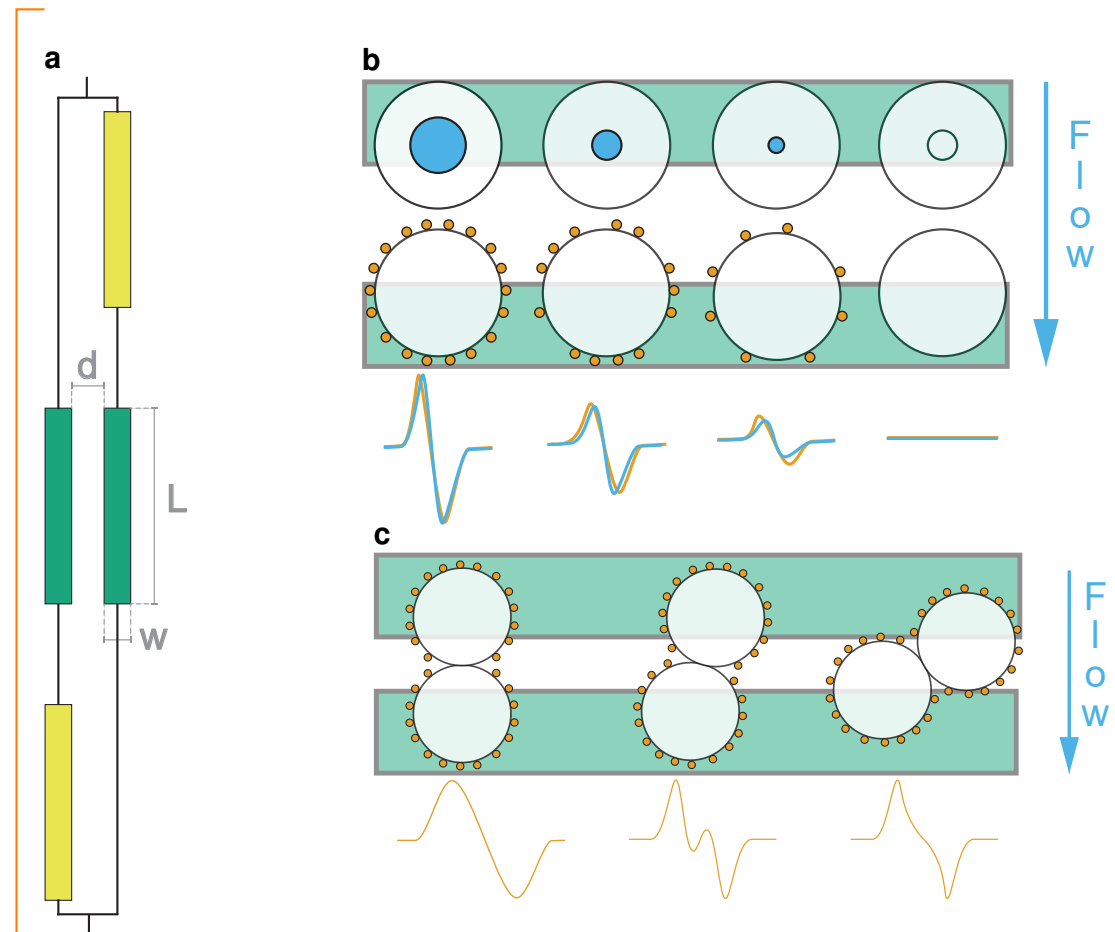


Figure 1: Particle Coverage Simulation

(a) Dimensions of the GMR Wheatstone bridge sensor: Distance d between both variable bridges (green), width w of a GMR-sensor, length L of a sensor. (b) Scheme of single cell simulation: The ideal magnetic dipole in the geometric center of a sphere (●) causes a signal deviation from the real cell signal with magnetic moment distributed on the cell surface. (●) (c) Signal shapes of different angles of two-particle aggregates lead to differing signal shapes.

al Similarity For
With Varying Bead
verages, Cross-Correlation
een single dipole with
magnetic moment and
ce covered with randomly
uted magnetic particles,
ulation of cell rolling veloc-
and forces

Parameter	Unit	Value	Explanation
w	m	2.0×10^{-6}	GMR width
l	m	30.0×10^{-6}	GMR length
d	m	14.0×10^{-6}	Distance between two sensors
R	Ω	250	GMR Resistance
V_p	mV	100	Supply voltage
$t_{free\ layer}$	m	7.0×10^{-9}	Thickness of free layer
M	$A\ m^{-1}$	2.0×10^4	Volume Magnetization
$V_{noise,rms}$	V	2.5×10^{-6}	Artifical noise
Sim. Space	m	$[-25 \times 10^{-6}, 25 \times 10^{-6}]$	Interval around sensor center

Table 1: Magnetic Simulation Parameters

Constants used inside the framework for the simulation of the magnetic field inside the GMR Wheatstone half bridge. The volume magnetization was adapted according to the simulated particle size.

1.1.2. Single Cell Signal

Aim of these simulations is to find a measure of how magnetic labeling of a cell affects signal shape and its subsequent analysis. A single cell with a surface coverage of 5 % to 99 % of a densely packed sphere was loaded randomly with MNPs at different sizes. Then, the previously explained rolling motion over the sensor bridge was simulated with the parameters specified in Table 1. After correlation of the resulting signal voltage to the reference dipole signal (Fig. 1b, ●) with three randomly MNP distributions, the dependency on the coverage was evaluated. As shown in the schematic Fig. 1b, an increase in signal peak amplitude but also in full width at half maximum (FWHM) at growing coverage was expected.

The expected behavior matches the data analysis (Fig. 2). Each two analyzed sphere diameters 4 μm and 8 μm with MNP sizes ranging from 20 nm to 2 μm , show a great standard error of the mean (SEM) at low coverage. This very probably is subjected to the momenta of single particles which play a greater individual role and hence influence the signal shape significantly because the overall dipole momentum in the sensor loses homogeneity.

Another observable effect is related to the MNP size. Absolute correlation differs from 20 nm to the ten and hundred fold diameter significantly. This can be related to the magnetic momentum per MNP as it is dependent on the volume - thus r^3 . However, for bigger magnetic particles this does not hold true because the composition changes from pure magnetite to a polymer shell with embedded oxide core at around 150 nm.

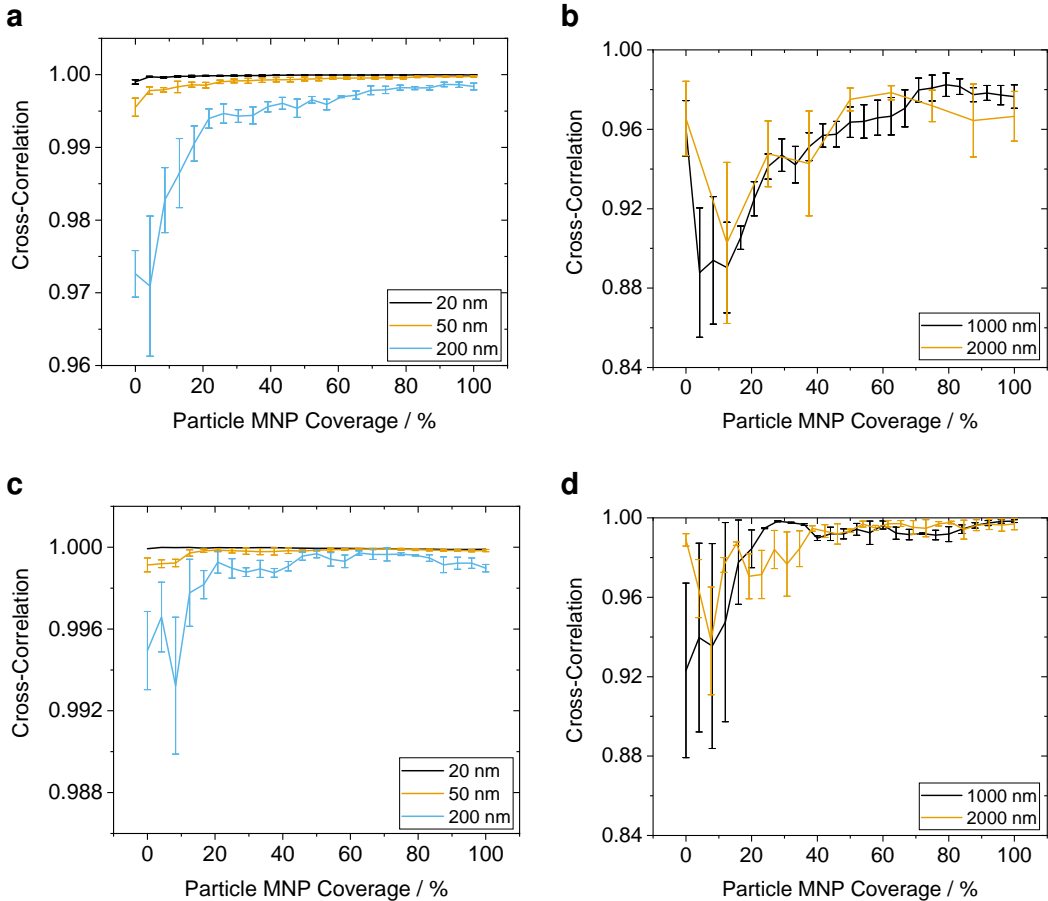


Figure 2: Coverage Dependent Signal Correlation

MNP coverage of a sphere with 4 μm (**a**, **b**) and 8 μm diameter (**c**, **d**) covered by magnetic particles ranging from 20 nm to 2000 nm. A cross-correlation increase which is inversely proportional to the MNP size can be observed.

Nevertheless, larger particles carry also greater magnetic momentum which brings also the aforementioned influence of single MNPs into consideration for that effect.

Also, the densely packed sphere surface can evidently carry more smaller than larger MNPs. This ranges from 641 600 MNP at 20 nm to 81 at 2 μm for a sphere radius of 4 μm and limits the maximum achievable momentum.

In reality, a maximum immunomagnetic label density depends not on the densely packed sphere but rather on the present antigens, and association or dissociation constants. Therefore, a complete saturation coverage is not achievable under physiological conditions. This leads to the fact that any possible momentum by deposition of 20 nm and 50 nm on a cell surface cannot be resolved from noise by this sensing setup.

Also, it can be seen that the correlation approaches a maximum obtainable value for every MNP size. Referenced for both simulated sphere diameters in (Fig. 3a), a inverse proportionality between correlation and MNP diameter is visible. The trend in respective maxima can be related to differences the magnetic momentum amplitude and coverage inhomogeneity.

Inter-sphere compared, maximum correlation shows also a significant decrease in for

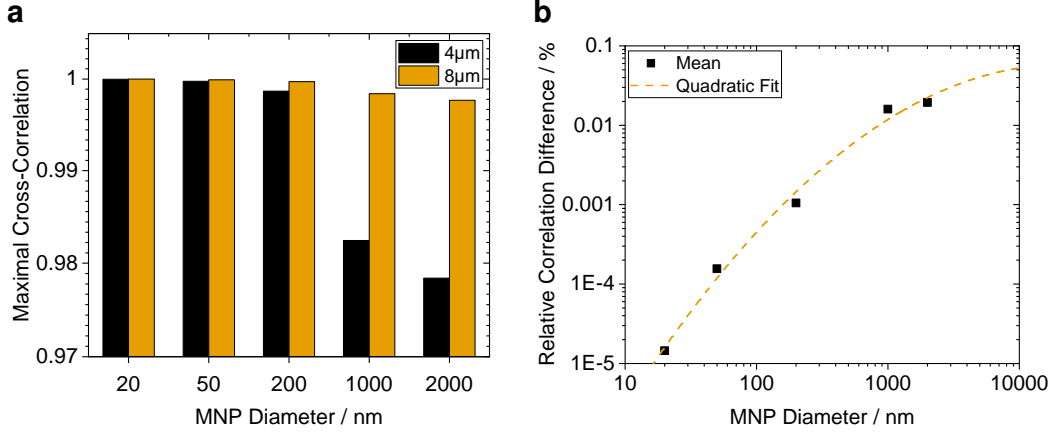


Figure 3: Maximal Cross-Correlation Differences

(a) Mean coverage at 99% for 4 μm and 8 μm spheres. A negative dependency on the MNP size can be explained by the ratio of magnetic momentum per unit surface and its homogeneous distribution across the whole surface.
 (b) Relative correlation error between 4 μm and 8 μm spheres with a quadratic fit. The quadratic behavior could be related to the relative surface area which can be occupied by magnetic momentum. (Adj. $R^2 = 0.992\,09$)

higher MNP sizes as the particle diameter itself increases. The relative error between both sizes - as computed in Eq. 1.5 - is depicted in Fig. 3b. Assuming a dependency on the available particle surface and subsequently the fraction which can be occupied by MNPs, a quadratic fit seems appropriate. (Eq. 1.6) The fit could indicate that a reference dipole cannot be discriminated from a cell at small MNP diameters while the correlation error becomes nearly constant at great MNPs.

$$\text{Relative Correlation Difference} = 1 - \frac{\max\{\text{Cross-Correlation}(d = 4 \mu\text{m})\}}{\max\{\text{Cross-Correlation}(d = 8 \mu\text{m})\}} \quad 1.5$$

$$\text{Relative Correlation Difference} = -0.385\,32 d_{MNP}^2 + 3.345\,74 d_{MNP} - 8.496\,29 \quad 1.6$$

1.1.3. Cell Aggregates

In another simulation, two 200 nm-MNP-covered spheres were attached to each other in differing angles and simulated flowing over the sensor. Signal similarity to a magnetic dipole in the center of a single reference sphere was computed by cross-correlation. As can be observed in Fig. 4, correlation is identical to a single sphere at low coverages when the magnetic momentum is high enough to form a uniform magnetic field. At occupancies greater than 50 %, the two attached cells have to be considered as individual dipoles in superposition and thus show a signal that carries small peaks in the center. This is shown schematically in Fig. 1c. In turn, this causes a high signal deviation from the reference and thus a low degree of correlation.

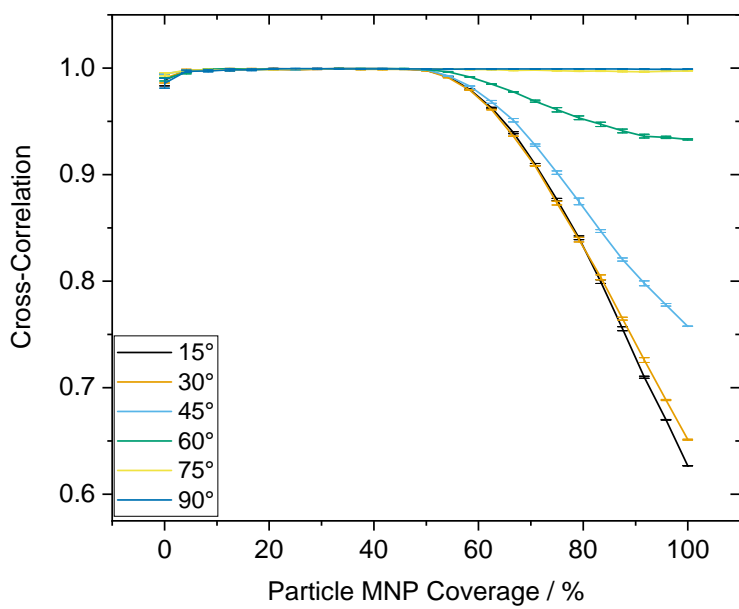


Figure 4: Signal Correlation between Two-Cell Aggregates At Shifting Angles

Two-Sphere aggregates are covered with 200 nm MNPs and simulated flowing over the sensor at differing respective angles. The SEM indicates a difference in cross-correlation of three truly random MNP distributions. For low yaw angles and high coverages, the aggregate's signal reflects rather two single dipoles in superposition than one quite homogeneous dipole. This causes a high signal deviation from the reference and thus a low degree of correlation.

1.2. The MRCyte Simulation Framework

In this work, also a analytical simulation framework that is capable of simulating the synergy of multiple microfluidic effects was developed. The comprehensive framework features magnetic, fluid dynamic and biochemical processes inside the utilized microfluidic channel which act on a particle. Foremost, material parameters was stored inside the “MRCyte” class, which range from channel and particle properties to binding and friction constants. Basic velocity, shear and magnetic field computations build the core of the presented program. Additionally, several dimensionless parameters such as the Stokes or Reynolds number (Re) or particle properties can be computed.

With that, simulations of the fluid dynamics that influence a single microbead as well as force-equilibrium computations for the same bead were carried out.

Capabilities - Simulation
over sensor, particle distribution
on surface, analysis of
GMRTTool data single and
differential, magnetic field per-

1.2.1. Fluid Fields inside the Microchannel

The simulation framework provided a quantitative generation of the Hagen-Poiseuille flow profile inside the microchannel with the numerical solution of ???. The simulated channel had dimensions (w x h x L) 700 μm x 150 μm x 15 800 μm . The flow rate was chosen at 80 $\mu\text{L min}^{-1}$.¹ Tubing as well as time dependent effects were neglected.

The simulated flow field (\mathbf{u}) for the whole channel cross-section can be observed in Fig. 5a. Due to the no-slip boundary condition, flow field (\mathbf{u}) is zero on the margin while the maximum of is reached in the geometric center. mean fluid velocity ($\bar{\mathbf{u}}$) in the channel ensues 12 670.84 $\mu\text{m s}^{-1}$.

In contrast, computation of the flow gradient in vertical direction and scaling with dynamic viscosity (η) yield the shear stress field.(Fig. 5c) As the curvature of \mathbf{u} is zero in the channel center and maximal at the edges, the shear stress reaches highest values symmetrically at the horizontal edges of the channel.² Resulting, the net viscous shear $\tau_{viscous} = \frac{\partial u}{\partial z}$ cancels out over the whole channel cross-section.

Additionally, \mathbf{u} and viscous stress tensor ($\tau_{viscous}$) acting on a 8 μm diameter bead on the channel bottom were analyzed.(Figs. 5b and 5d). In the proximity to a wall and due to the applied boundary conditions, $\tau_{viscous}$ enclosed by the bead surface is non-linear. Thus, the mean fluid velocity exposed to the bead amounts in $\bar{\mathbf{u}}_p = 2241.59 \mu\text{m s}^{-1}$, whereas $\bar{\tau}_{viscous, p}$ strains with 4.93 dyne cm^{-2} .

¹ in accordance with the experimentally determined value

² Because the horizontal components of the gradients were neglected graceless

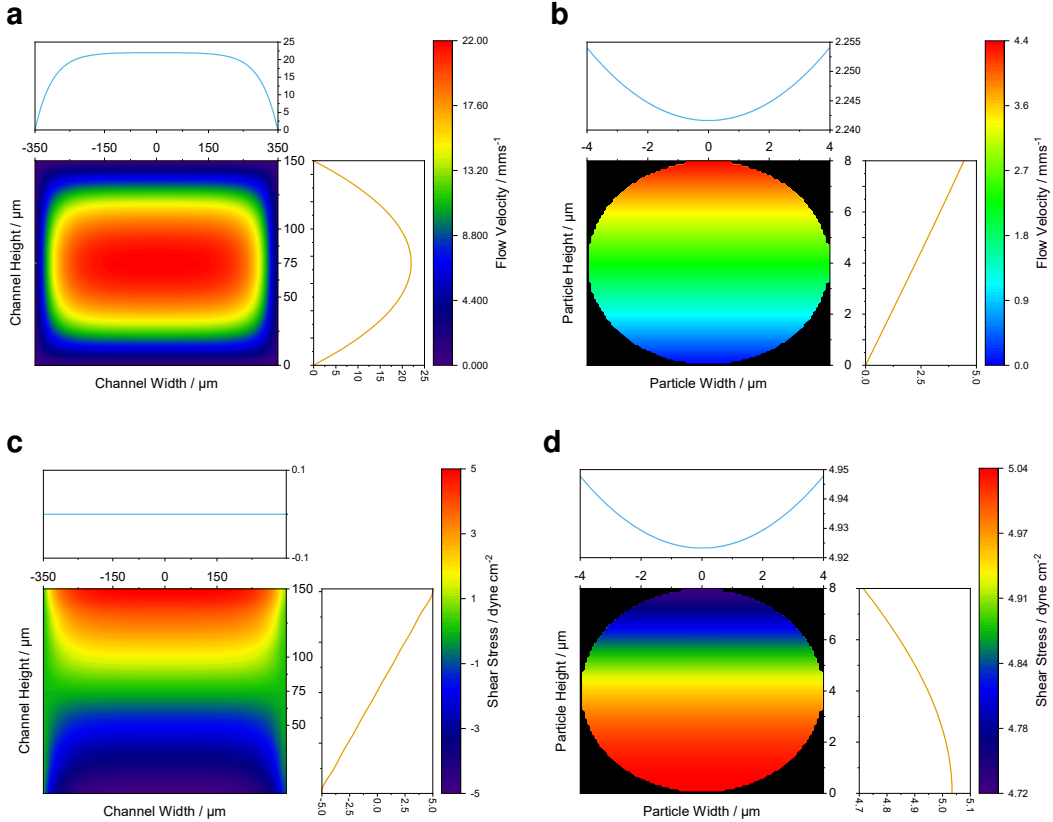


Figure 5: Flow Field and Shear Stress Simulation of the utilized Microchannel

Flow (a) and vertical shear (c) field inside the microchannel with dimensions ($w \times h \times L$) $700 \mu\text{m} \times 150 \mu\text{m} \times 15800 \mu\text{m}$ for a flow rate of $80 \mu\text{L min}^{-1}$ and with neglected tubing effects. The subplots on the right and top side show the mean horizontal and vertical profile in $0 \mu\text{m}$ width and $75 \mu\text{m}$ height, respectively. (vertical: —, horizontal: —) Due to the no-slip condition, the velocity at the walls equals zero and the shear is maximal. The maximum of the Hagen-Poiseuille profile is located in the channel center. Over the cross-section the mean flow velocity \bar{u} equals $12670.83 \mu\text{m s}^{-1}$. Resultingly, the net horizontal viscous shear $\tau_{viscous} = \frac{\partial u}{\partial z}$ cancels out over the whole channel cross-section.

Flow (d) and vertical shear (d) field acting on a $8 \mu\text{m}$ diameter bead on the channel bottom. The mean fluid velocity trapped by the bead profile results in $\bar{u}_p = 2241.59 \mu\text{m s}^{-1}$, whereas the viscous shear strains with $\tau_{viscous} = 4.93 \text{ dyne cm}^{-2}$

1.2.2. Modelling the Force-Equilibrium of a Rolling Bead over a Biofunctionalized Surface

nice intro

With the supplier's parameters of a 8 μm micromer-M bead (micromod Partikeltechnologie GmbH, Rostock) the corrected drag force on a bead on the bottom of the standard utilized microchannel resultes in 463.65 pN for 80 $\mu\text{L min}^{-1}$.

If the bead was functionalized with biotin under negligence of the differential equations for the association constants, the number of interacting groups would result in the present surface charges. Surface charge density resultes in 1 $\mu\text{mol g}^{-1}$ of $-\text{COOH}$ (carboxyl) and $-\text{NH}_2$ (amine) beads as of the supplier's datasheet. Hence, a fully saturated bead is covered in 177 500 biotin molecules.

The streptavidin coverage of the channel floor was modeled in excess over the biotin ligands. The penetration depth was estimated by the size of several monolayers protein. As described by Wu and Voldman [9], an approach of 30 nm is a reasonable quantity. In turn, the surfaces were in contact with 1.51 μm^2 which constitutes 0.75 % of the 8 μm bead surface. This reveals that 1329 biotin molecules can interact with the floor. A summation of the protein-bond force ($\mathbf{F}_{protein}$) at 5 pN to 150 pN per streptavidin-biotin bond yields the resulting adhesion force with a magnitude of 6.7 nN to 199 nN.[74]

The binding force is in the same range as the perpendicular magnetophoretic force caused by the permanent magnet under the sensor chip ($\nabla\mathbf{B} = 10 \text{ T m}^{-1}$) as well as by the nickel-iron chevron structures on the chip ($\nabla\mathbf{B} \approx 5 \text{ kT m}^{-1}$). Clearly, in the near-field approximation the nickel-iron structures dominate magnetic force (\mathbf{F}_{mag}) (??). With the manufacturer given saturation momentum of one particle (1.12 pA m²), the magnetic attraction force eventuates in 5.6 nN.

$$\mathbf{F}_{\parallel} = \mathbf{F}_{drag} - C_{rr} \cdot (\mathbf{F}_{mag} + \mathbf{F}_{protein} + \mathbf{F}_{grav} - \mathbf{F}_{shear}) \quad 2.7$$

$$C_{rr} = \sqrt{\frac{z}{d}} = \sqrt{\frac{30 \text{ nm}}{8 \mu\text{m}}} = 0.0612 \quad 2.8$$

In order to merge this analytic force balance, all remaining forces have to be projected into the direction of Stoke's drag force (\mathbf{F}_{drag}). (Eq. 2.7) This is achieved by the introduction of the rolling resistance factor (C_{rr}) for a perfectly elastic surface. (Eq. 2.8) In a first order approximation, the factor depends only on the approach (z) and the bead diameter (d). However, scientific literature about the rolling resistance of microbeads on microfluidic or protein covered surfaces does not exist yet to confirm this macroscopic factor for the microscale.

Scaling all orthogonal forces to the Stoke's drag force with C_{rr} yields a net positive result (154.08 pN) for an unfunctionalized surface ($\mathbf{F}_{protein} \stackrel{!}{=} 0$) which indicates a rolling

motion in flow direction. Notwithstanding, above a critical interaction number of 16 to 503 biotin-streptavidin bonds - for the respective release forces of 5 pN to 150 pN per linkage - the particle resists Stoke's drag force and adheres to the surface.

This behavior will be exploited in further measurements for "bead loss experiments" in order to measure a concentration difference with different degrees of biotinylated beads.

1.3. Reference Bead Surface Functionalization

After simulation of their respective coverages, biotin was titrated on 8 μm reference beads with two different surface terminations in order to selectively bind MNPs with the counter-agent streptavidin to the surface. First, amine-microbeads were modified by sulfo-NHS-biotin. Second, carboxyl-beads were coated by amine-PEG₂-biotin via EDC-NHS-activation. On the same beads Anti-IgG1-PE antibodies were titrated after the same coupling chemistry.

Subsequently, biotin-coated beads were analyzed in the flow cytometer in the by staining with Atto-488 (Ex: 500 nm, Em: 520 nm) coupled streptavidin. The antibody was already industrially modified with phycoerythrin (PE) and measured at 488 nm excitation and 585 nm emission wavelength. The gating was standardized by the strategy found in ??, ???. Subsequently, the median fluorescence intensity (MFI) was computed and fitted with a Hill-function.(??) Stability of carboxylated and aminated beads and subsequently their respective modification protocols was evaluated for 12 days.

1.3.1. Amine-Surface Biotinylation

As first approach, polystyrene copolymer microbeads with 8 μm diameter were functionalized by (sulfo-)NHS-biotin after a standard protocol. A titration of the biotin reactant yielded a varying surface coverage as shown in Fig. 7a. During this one-pot-reaction, the water-soluble sulfo-NHS-biotin forms an R₁—CONH—R₂ (carboxamide) linkage with the primary amine and 1-hydroxy-2,5-dioxopyrrolidine-3-sulfonate splits off as byproduct.

As can be seen from the SEM error-bars from the plot 7a, which were constructed from three true biological replicates, this process is highly reproducible. Therefore, an surface coverage in different grades of biotinylation could be obtained accurately with a adjusted coefficient of determination (adj. R^2) of 0.981 for the resulting Hill fit (- - -).

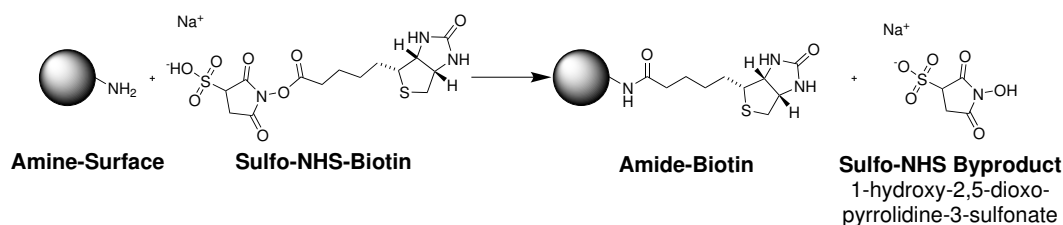


Figure 6: Amine Bead Modification with Sulfo-NHS-Biotin

An amine terminated bead brought into reaction with sulfo-NHS-biotin. Both form an amide linkage and bind biotin covalently to the surface. As byproduct the sulfo-NHS-ester splits off.

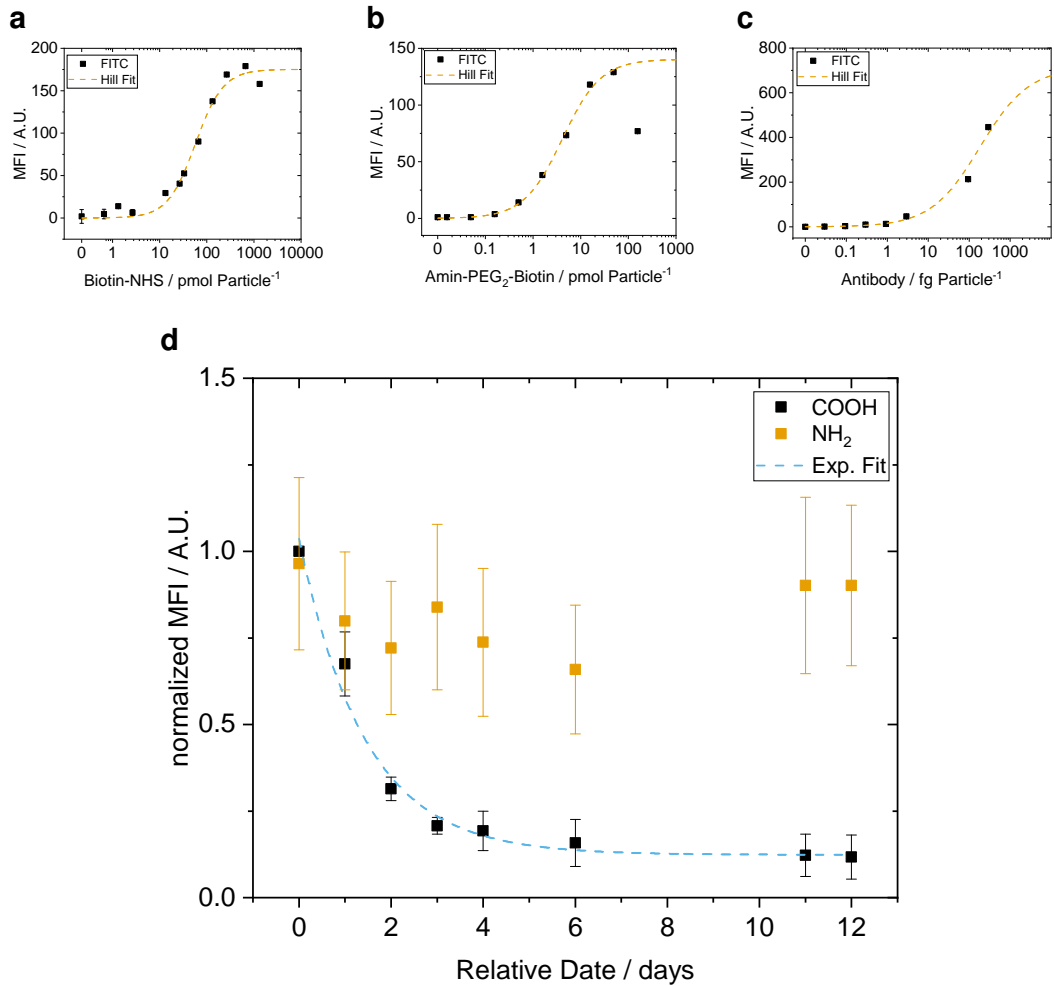


Figure 7: Titration of Biofunctional Molecules on 8 μm Particles

Titration curves of NHS-biotin (a), Amin-PEG₂-Biotin (b), and Anti-IgG1 (c) with their respective Hill fits. The corresponding fit parameters as well as the goodness factor are shown in Table 2a. (d) Stability analysis of functionalized carboxyl and amine beads over 12 days. The carboxylate particles show an exponential decrease with a half-life of 1.43 days as determined by the exponential fit. The respective parameters are shown in Table 2b.

a				b		
Param.	Hill 7a	Hill 7b	Hill 7c	Param.	Exp. 7d	
V_{max}	175.216 19	140.391 53	713.836 43	A	0.912 63	
k	57.367 13	4.126 61	182.830 11	τ_{decay}	1.425 57	
n	1.474 88	1.074 93	0.724 58	y_0	0.123 69	
Adj. R^2	0.981 21	0.997 22	0.992 26	Adj. R^2	0.966 55	

Table 2: Fit Parameters of Biotinylation

(a) Coefficients for the Hill fits in Figs. 7a to 7c (b) Exponential fit coefficients for the stability analysis in Fig. 7d

Carboxylate-Surface Functionalization

In a second approach, particles with opposite partial surface charge, mediated through carboxyl groups, have been functionalized. In turn, particles were pre-activated in 3-(Ethyliminomethyleneamino)-N,N-dimethylpropan-1-amine (EDC) and 1-Hydroxy-2,5-pyrrolidinedione (NHS) in 2-(N-morpholino)ethanesulfonic acid (MES)/MES buffer with Tween 20 (MES) buffer. There are two distinct reasons for the usage of MES based buffers rather than phosphate buffered saline (PBS) or MACS running buffer (MACS). First, EDC has its reactive maximum at pH 5 to 6. Second, buffers containing primary amines (TRIS / glycine) or carboxyls (acetate / citrate) will quench the reaction and therefore limit the efficacy.

Afterwards, the beads were washed carefully and incubated with amine-PEG₂-biotin. Here, poly(oxyethylene) (PEG) indicates a hydrophilic spacer arm between both functional groups and in this case has length of a two units. The full functionalization procedure is explained in more detail in ??.

As shown in Fig. 7b, particles were functionalized equally compared to carboxamide surfaces. However, the stability of carboxyl particles yields 1.43 days half-life in a continuous measurement over 12 days with a subsequent exponential fit. Additionally, both procedures show an outlier at high concentrations which could not be explained during the course of this thesis.

Third, carboxylated particles have been also functionalized with the Anti-IgG1-PE antibody. Again, a Hill-shaped titration curve was achieved, but due to the costly reagent a saturated surface coverage was not reached. (Fig. 7c)

Therefor, the fit curve has to be interpreted cautiously. Although it converged and represents the data with an adj. R^2 of 99.2 %, the goodness of fit determined by the reduced χ^2 statistic results in a value of 278.1 which indicates an underestimation of the error variance.

1.4. Concentration Measurements in MRCyte

Driving factor for the concentration measurement is the absolute count of immunomagnetically labeled cells in diluted or whole blood which is not possible in today's optics-based devices due to the excess of red blood cells (RBCs). [87] Therefore, with the in ?? described sensor setup, absolute concentrations of magnetic reference beads were attempted to measure.

Consequently, beads with acrylate surface were pumped through a microfluidic channel with a permanent magnet underneath. The magnet drew every magnetic particle to the ground, where they were focused on the sensor bridge and subsequently measured there. From the received signal several parameters such as peak amplitudes, locations, zero-crossings, and relative distances between each other were computed. (Fig. 8) However, for a concentration measurement mostly the correct detection of a signal from the noisy stream or from a superposition of multiple simultaneously measured particles was critical. The related error sources and countermeasures will be elaborated in Sec. 1.4.1.

By measuring the absolute concentration with a commercially available flow cytometer (MacQuant 10, Miltenyi), a reference bead count was established. In a pre-test, beads were taken directly from the microcentrifuge tube, after pumping through a syringe, and after pumping through a syringe with 10 cm of connected tubing (ID 0.5 mm, RS Chemicals). Afterwards, they were counted in the flow cytometer in equal volumes. Additionally, two different buffers - MACS and PBS - and two different surface terminations were used. Both buffers are based on phosphate buffered saline (PBS). Notwithstanding MACS contains 2,2',2'',2'''-(ethane-1,2-diyl)dinitrilo)tetraacetic acid (EDTA) as chelator for divalent ions, Tween 20 - a non-ionic surfactant -, and an azide-based stabilizer. Hence, the wetting of surfaces and the electrostatic interactions of these buffers differ. The same properties were varied on the bead surface by choosing acrylate- and biotin-terminated beads.

In Fig. 9, a trend (without statistical confidence) can be observed that shows a decrease in particle counts after every additional surface which beads could potentially interact with. In term, a correct count in absolute numbers seems out of range. However, a calibration of the system with the flow profile inside the channel to compensate for losses subjected to connectors and magnetic enrichment structures was carried out successfully.

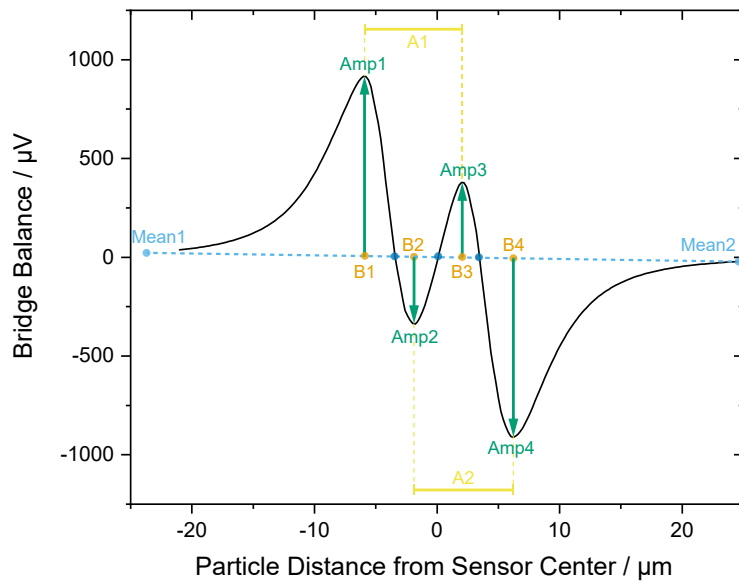


Figure 8: Example Signal of Magnetic Measurement

Signals generated from the Wheatstone bridge sensor setup feature a certain shape which allows for several measures. In case the overall signal stream carries a constant or linear offset, it is scaled to the means before and after the detected peak pattern. (Mean1, Mean2) The x- and y-positions of each peak are denominated by B1-4 and Amp1-4, respectively. The crossings of the signal through the linear connection of both means are denominated by n1-3 (in the figure by ●). Further, the difference between the equally oriented peaks B3-B1 and B4-B2 give a measure for the homogeneous movement of the measured object and are called A1 and A2 each. From these values the overall velocity v can be approximated because the GMR bridge distance (d_{GMR}) and sampling frequency (f_s) is fixed precisely. Analogously, the magnetic diameter of a dipole is computed by the mean of the differences B2-B1 and B4-B3.

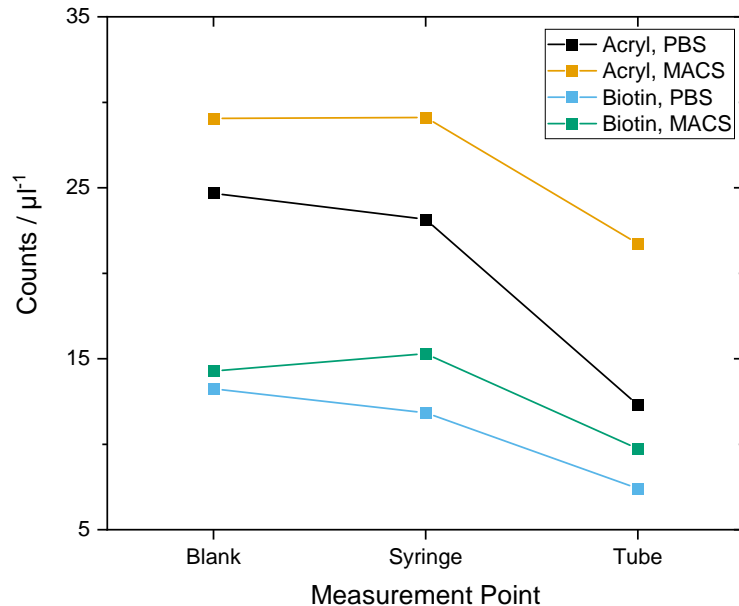


Figure 9: Bead Loss Evaluation in Connectors

Bead concentrations measured in equal volumes in the flow cytometer after being pumped through a syringe or a syringe with connected tubing. The blank sample was measured directly from the stock solution. Additionally, electrostatic and surface tension related effects were resolved by the usage of different buffers and bead surfaces.

1.4.1. Measurement Error Sources and Calibration of Flow Field

In order to account for the bead losses due to the tubing connectors, the Hagen-Poiseuille flow profile, and magnetophoretic enrichment structures, the measured bead concentration was corrected in two different approaches.(Eq. 4.9) On the one hand side, the typical assay correction to the ground truth by a constant linear fit correction factor (C_{const}) computed from the blank population was established. On the other side, a velocity correction factor ($C_{velocity}$) compared the mean fluid velocity (\bar{u}) to the bead velocity (v_c).

$$c_{beads, expected} = c_{beads, measured} \cdot C \quad 4.9$$

The C_{const} relates a reference count in the optical flow cytometer to the measurement in the magnetic flow cytometer.(Eq. 4.10) Equally-adjusted bead concentrations in the samples allow for a correction to the reference system. However, for an assay usage the initial concentration of beads either has to be known precisely or has to be irrelevant, for example in regards of a standardized measurement procedure. Besides, C_{const} provides a reliable and generalizable option for correction.

$$C_{const} = \frac{c_{beads, standard\ procedure}}{c_{beads, MRCyte}} \quad 4.10$$

$$v_c = 2 d_{gmr} \frac{f_s}{n_3 - n_1} \quad 4.11$$

$$C_{velocity} = \frac{\bar{u}}{v_c} = \frac{Q}{A \cdot v_c} \quad 4.12$$

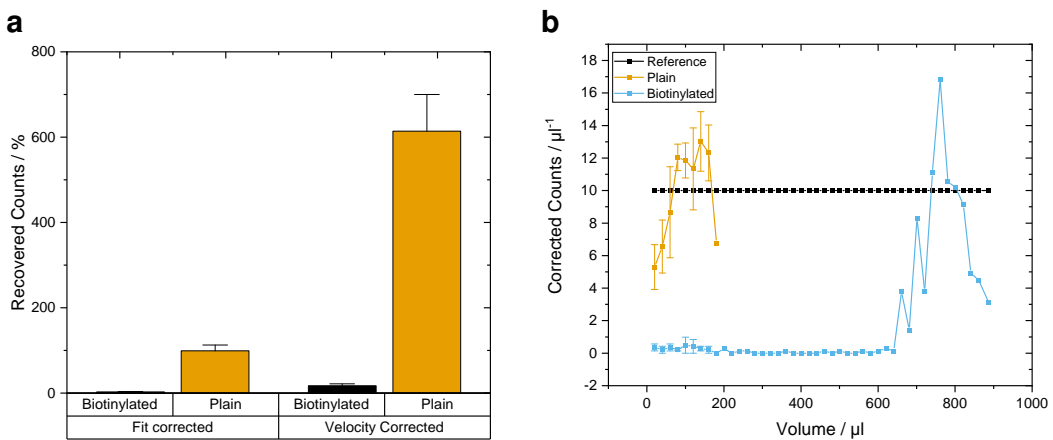


Figure 10: Error Sources in Concentration Measurements

(a) Robustness evaluation of the both correction factors C_{const} and $C_{velocity}$ for protein coated surfaces. The mean and SEM of plain and biotinylated measurements show a high deviation from physically reasonable expectations when corrected for the velocity (right). In contrast, C_{const} can intrinsically correct only well below 100 %. (b) Mean and SEM of a fit-corrected bead capture experiment with several error sources. Initially, the magnetophoretic structures have to be filled and thus decrease the plain count for the first 100 μL . (—) Additionally, the high deviation offsets the correction factor so that the stable measurement from 100 μL to 200 μL lies now above the ideal reference. In contrast, the biotinylated beads are captured by the surface functionalization and hence a very low concentration is measured. However, a steep rise with pulsations can be observed when the surface is saturated with beads and the particles begin to flow over the sensor in bursts. (—) The abrupt decline to the end of the measured volume is most probably related to sedimentation effects inside the emptying syringe.

The $C_{velocity}$ relates the effective particle velocity to the total fluid velocity in order to eradicate flow profile provoked effects.(Eq. 4.12) Whereas \bar{u} was determined by flow rate (Q) through a cross-sectional area (A) of the channel, v_c was analyzed from the measured signal stream. Here, the intrinsic GMR bridge distance (d_{GMR}) was divided by the time difference where the bead passed exactly over a GMR-element.(Eq. 4.11) These specific timepoints are visible as dimensionless zero-crossings n_1 and n_3 in the signal and can be converted by scaling with the sampling frequency (f_s) into the time domain.

However, if the bead velocity is not solely dependent on fluid dynamic effects - espe-

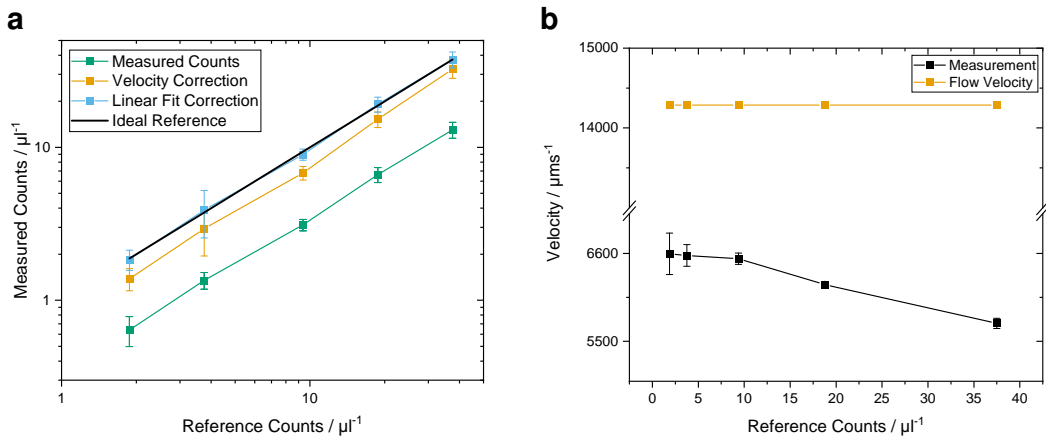


Figure 11: Absolute Concentration Measurements

(a) Mean and standard deviation of the concentration measurement from three independent measurements. The uncorrected measurement shows a highly reproducible and linear count over the dynamic range of almost two decades. (—■—) The ideal reference from the flow cytometer is depicted in (—). Correction with $C_{velocity}$ (—■—) yields at a factor of 2.261 09 which is 21.7 % more imprecise than C_{const} at $2.888\ 33 \pm 0.080\ 75$. (—■—) (b) Mean and SEM of the v_c estimation from the signal. For higher concentrations, the measured velocity becomes inaccurate thus distorts the correction factor.

cially in the light of surface functionalizations - $C_{velocity}$ can not be applied to experiments robustly. This is depicted in a sample experiment with a protein covered surface in Fig. 11a. By definition, the C_{const} can not be well above than 100 % whereas the count correction by $C_{velocity}$ differs by 600 % through variations in the velocity measurement.

An adaptation of these corrections to real measurements are depicted in Fig. 11. In a measurement where 300 μL were dispensed into the magnetic flow cytometer with a defined particle concentration the counts were analyzed and corrected according to above. This time, the channel had a cross-section of 700 $\mu\text{m} \times 50 \mu\text{m}$ (w x h) and flow rate (Q) was set to 30 $\mu\text{L min}^{-1}$.

Apart from a reproducible count over the dynamic range of almost two decades, both correction factors ameliorated the present data. C_{const} amounted in an optimum 2.89 ± 0.08 while $C_{velocity}$ centered around a mean of 2.26. Consequently, the velocity correction was misguided by 21.7 % for the advantage of requiring no *a priori* knowledge about the measurement.

Another peculiarity of $C_{velocity}$ can be observed in Fig. 11b. While the analyzed velocity is stable for less than $10 \mu\text{L}^{-1}$, a linear decrease is visible for higher concentrations. This is a consequence when signals of beads start overlapping if these are flowing over the sensor in a close vicinity. Hence, the disturbed signal sensitizes the parameter reconstruction to errors such as false peak-identification.

1.4.2. Concentration Measurement in Diluted Whole Blood

The same concentration measurements from before were now carried out in whole blood samples. Here, the reference count can be attained only below the experimentally determined critical concentration around $10 \mu\text{L}^{-1}$. (Fig. 12) An insignificant discrepancy could be perceived in different volumetric blood to buffer dilutions of 1:1 and 1:20, respectively. This provides evidence for the measurement's independence from the blood concentration in buffer.

However, a significant difference between counts was discovered between a $150 \mu\text{m}$ high channel, where $C_{velocity}$ can be determined accurately, and a $50 \mu\text{m}$ high channel, where the correction yields a great error to the reference. This may be subjected to an increased probability of collisions from beads with blood cells and hence a decreased velocity which in turn leads to a higher correction factor. Another explanation approach could be the transition from *Newtonian* to *Non-Newtonian* fluid dynamics in smaller cross-sections, which could likewise be influenced by the Fåræus effects mentioned in ??.

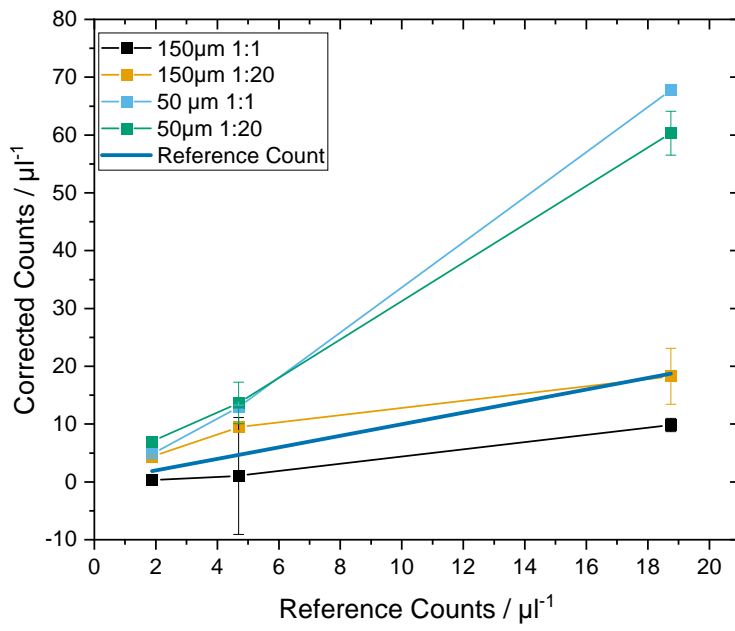


Figure 12: Absolute Concentration Measurement in Blood Samples Under Varying Channel Height

Velocity corrected concentration measurements for two different blood dilutions and channel heights. While $C_{velocity}$ works for high channels in all tested concentrations, it does not work for high concentrations in $50 \mu\text{m}$ high channels. This is probably a result of bead-cell collisions and the resulting path interruption.

1.4.3. Surface Magnetization of Biofunctionalized Beads

Here, the previously surface-modified polystyrene beads were magnetized with MNPs and counted in the magnetic flow cytometer. Originally, four different magnetic nanoparticles have been tested. Albeit, both nanomag-D-spio 100 nm (micromod Partikeltechnologie GmbH, Rostock) and dynabeads MyOne Streptavidin C1 1 μm (ThermoFisher scientific, Waltham, USA) showed inconclusive results.

First, BNF-Dextran-redF 100 nm (micromod Partikeltechnologie GmbH, Rostock) were attached to the non-magnetic beads after the protocol in ???. Then the magnetizability was examined qualitatively in a magnet stand. Thereby, the particles were considered magnetically labelled if a pellet was visible after 10 min. Afterwards, the concentrations were measured with the optical flow cytometer and adjusted to $10 \pm 1 \mu\text{L}^{-1}$ accordingly.

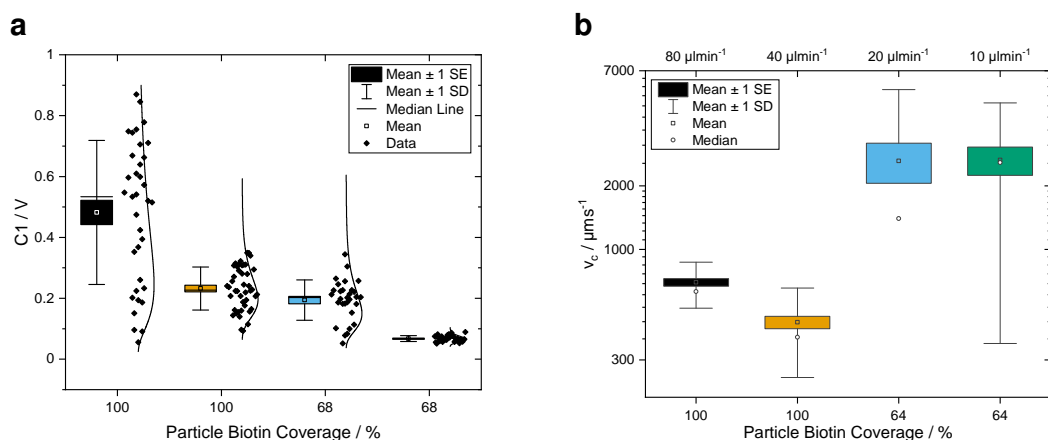


Figure 13: Bead Coverage Assay with BNF-Dextran-redF-100 nm
(a) 1. $80 \mu\text{L min}^{-1}$ 2. $40 \mu\text{L min}^{-1}$ 3. $20 \mu\text{L min}^{-1}$ 4. $10 \mu\text{L min}^{-1}$ (b) $d = 8 \mu\text{m}$

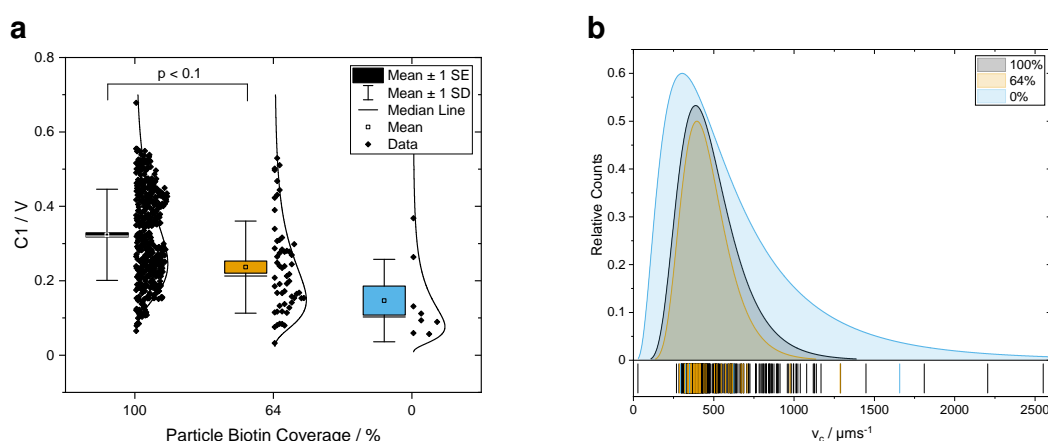


Figure 14: Bead Coverage Assay with OceanNanotec 50 nm
Mean from 3 different particle distributions at maximum coverage, SEM(a) $d = 4 \mu\text{m}$ (b) $d = 8 \mu\text{m}$

1.4.4. Count Stability

In this section the results of beads rolling a neutravidin-covered channel surface will be discussed. In order to measure the interaction properties diligently, beads were functionalized with biotin at several saturation degrees ranging from 0 % to 100 % total coverage of the available surface charges. Measurements for absolute counts as well as their time stability were carried out at $80 \mu\text{L min}^{-1}$ in a microchannel with cross-section $700 \mu\text{m} \times 150 \mu\text{m}$ (w x h). Fig. 15a shows the absolute, linearly corrected counts determined by the magnetic flow cytometer, with a defined particle concentration of $7.8 \mu\text{L}^{-1}$ to $10 \mu\text{L}^{-1}$. Clearly, a significant yes-no answer can be established by fully- vs. non-functionalized beads. Also, this measurement was highly reproducible with three different chip setups and measurement days. For approximately $\frac{2}{3}$ biotinylated beads, a gradation in counts can also be observed. However, due to the instability of the channel surface over the course of many sequential measurements, additional experiments have to be conducted to reinforce these results.

An evaluation of the time-domain distribution of the counted beads shows a very stable baseline for fully biotinylated beads with a recovery in the single digit range per unit volume. In the negative control of unbiotinylated beads, also a noisy mean count around 100 % can be observed.³

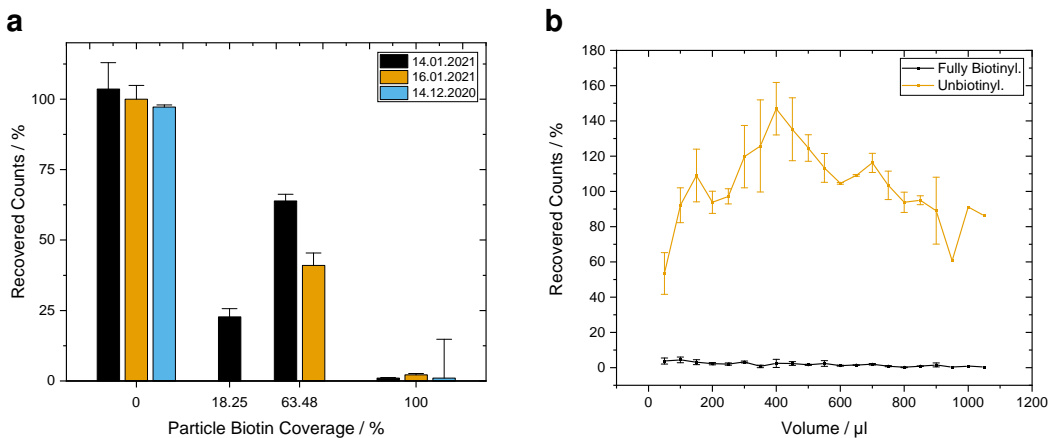


Figure 15: Reproducibility of Concentration Measurements with Saturated Neutravidin Surfaces

Biological replicates of concentration measurements with the magnetic flow cytometer. The channel surface was modified with 1 mg mL^{-1} neutravidin over night. (a) Mean and SEM of C_{const} adjusted counts for various biotinylation degrees. (b) Time series of the mean from the three measurements on the left. Biotin-beads are captured completely, thus very few counts are detected. (—) The unbiotinylated sample shows the initial ascent due to the in Sec. 1.4.1 discussed error which is related to the filling of the magnetophoretic structures. (—)

³ The shown data corresponds to the mean of three measurements from Fig. 15a

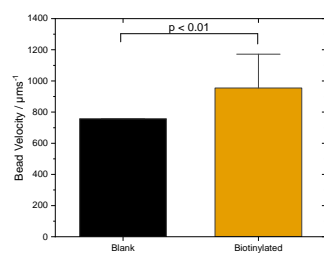


Figure 16: Measured Bead Velocity

Not sure what to say about velocity itself. Maybe remove $p < 0.01$

1.4.5. Differential Counting Setup

With regard to the necessity of correction factors in order to resolve the ground truth of a concentration measurement, a different magnetic flow cytometer setup has been evaluated. Here, two fully assembled sensors with printed circuit boards (PCBs) were stacked on top of each other and connected in series. This was expected to yield two beneficial effects.

First, one permanent magnet underneath the lower sensor chip should supply both chips with enough gradient field to pull beads to the respective channel bottom. Second, simultaneous signal acquisition should act on the one side as a time-of-flight detector with a relatively long transport distance. On the other side, a differential concentration measurement was envisioned between both chips. Therefor, the hypothetical optimum parameter set could be reached when the relative concentration measurement yielded identity:

$$\frac{c_{\text{top sensor}}}{c_{\text{bottom sensor}}} = 1 \quad 4.13$$

The system comprises of two separately assembled sensor PCBs with nylon spacers between the positional screws.(Fig. 17) A 3 mm hole was drilled into the top PCB carefully between the strip lines to minimize the tubing length from the top chip outlet to the bottom chip inlet. After the build-up of the differential counting system,⁴ the hysteresis of both sensor elements was maximized for sensitivity and the concentration was measured against a reference from the optical flow cytometer.

Sensitivity Calibration

Initially, the permanent magnet was adjusted in three linear directions in order to maximize the magnetic sensitivity of both Wheatstone bridges. Schematically, this can be envisioned as a placement of the whole top as well as the whole bottom bridge configuration into the operational range of the magnet, which is indicated by the blue triangle.

Then, the hysteresis of both outermost and one centered sensor was optimized for their full coverage and sensitivity. The recorded values for a sole optimization of the top or bottom sensor array with a height variation of the utilized nylon spacers are shown in Figs. 17b and 17c. Apparently, the optimized sensor exhibits a monotonously higher magneto-resistive effect (MR effect) than the disregarded bridge. Nevertheless, the complete sensor setup features a MR effect well above 7.2 % which is acceptable both for measuring immunomagnetically labeled cells and magnetic microbeads. Furthermore, the homogeneity of the interspersing magnetic field can be monitored in the triangular shape of every acquired curve in the sensitivity plots. As the field vectors of magnetic flux density (\mathbf{B}) start to disperse at the outsides of the illustrated blue area in Fig. 17c, the outer sensor regions are not located completely inside a uniform field and get distracted by non-perpendicular field components.

⁴ as described in ??

Additionally, no influence of any spacer height could be discovered. The difference in MR effect varied insignificantly in $0.14 \pm 0.60\%$ of MR effect.

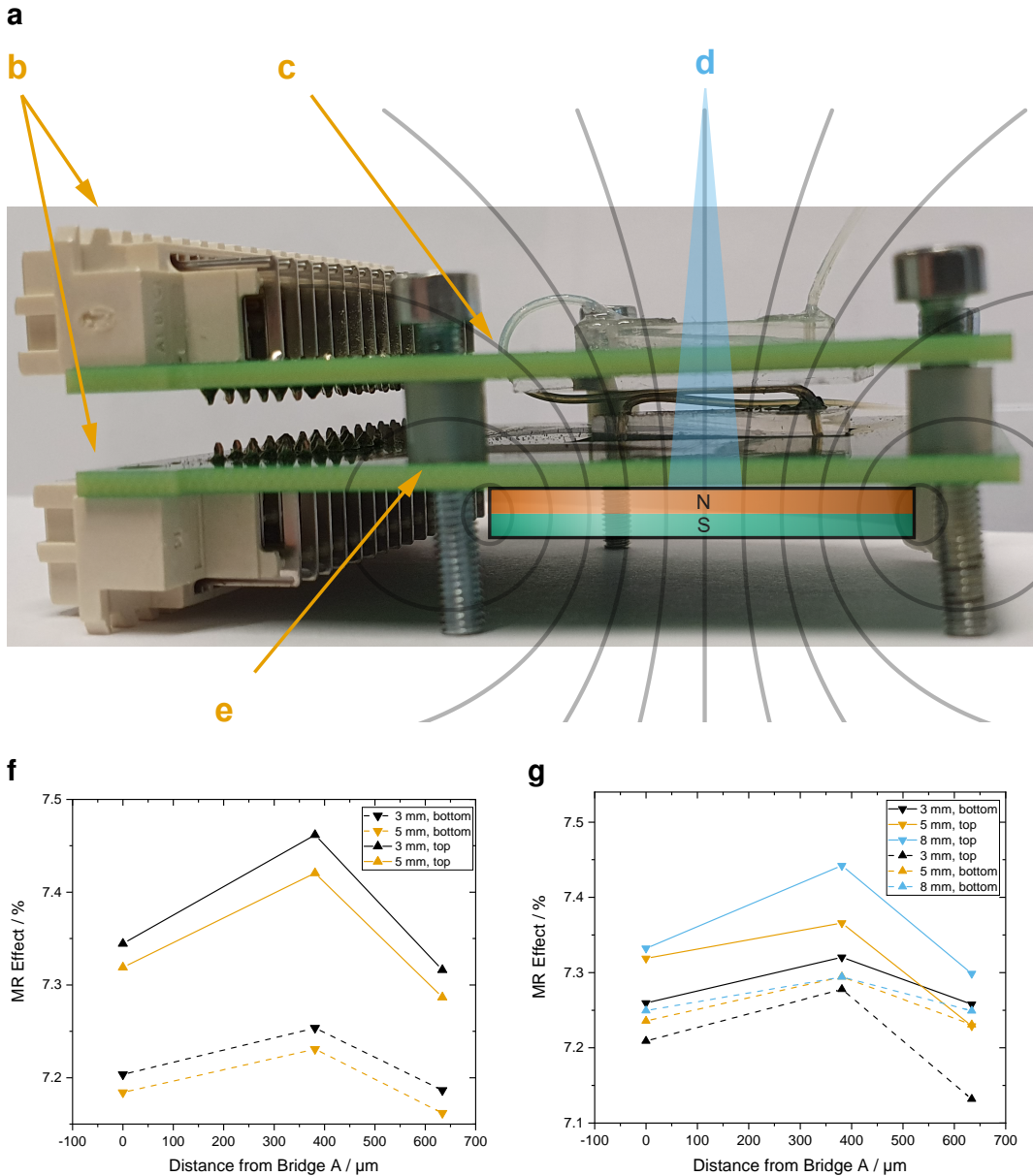


Figure 17: Hysteresis Calibration for Stacked PCB Setup

(a) Differential measurement setup: the system comprises of two separately assembled sensor PCBs (b) with nylon spacers (e) between the positional screws. (d) The field line density respectively the area with negligibly differing field vectors is shown in the blue triangle. Because the adjustment is always carried out for a single bridge at once, this causes a systematic error.

The magneto-resistive effects of both sensors, calculated from their hystereses, are depicted for top and bottom sensors, respectively. Whereas the hysteresis was optimized for the centered sensor bridge (D or E) on the top sensor in (f), it was optimized for the bottom sensor in (g). Additionally, the height of the nylon spacers was varied from 3 mm to 8 mm but showed no statistical correlation.

Concentration Measurement in Buffer Solution

Due to the single utilized permanent magnet for two sensors, another field related issue arose during concentration measurements. This requires a step back inside the general functionality of the magnetophoretic enrichment:

Any bead flowing at an arbitrary position in the microchannel experiences a positive magnetic force by the gradient of the magnetic flux density caused by the permanent magnet which pulls perpendicular to the bottom surface. Upon coming in close proximity to the lower boundary, a gradient provoked by the lithographic nickel-iron structures starts to gain strength with the third power of the distance. This causes the beads to attach to the bottom firmly and enforces their rolling behavior. However, a fragile equilibrium between magnetophoresis and drag has to be maintained slightly in favor of Stoke's drag force for a continuous rolling motion. This ideal state is a narrow space in between two boundary cases.

First, if drag force outnumbers magnetophoresis, the beads will not migrate to the channel bottom in the top chip and hence cause a depressed concentration measurement on top. Second, if magnetophoresis outnumbers drag so that particles flow steadily in the top channel, the beads in the lower channel will stop rolling and adhere statically. In effect, the lower concentration measurement is compromised.

In order to find the flow rate for the optimal ratio between drag and magnetic force, mea-

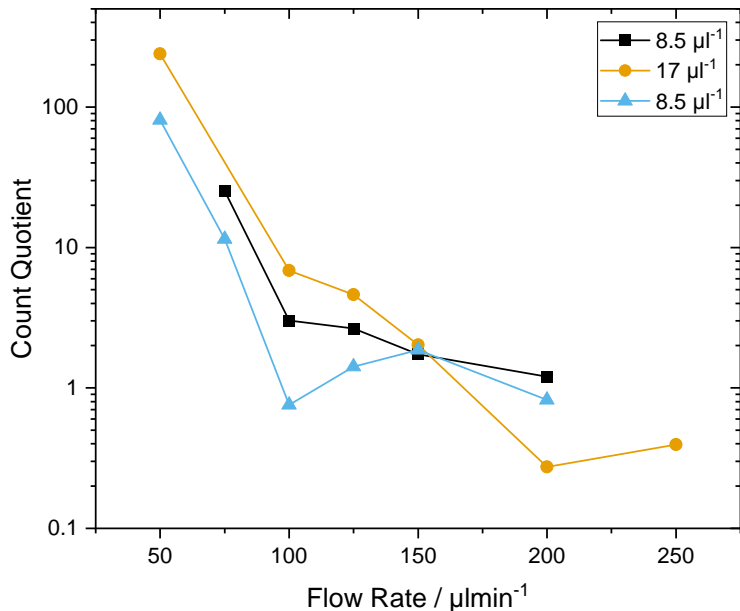


Figure 18: Optimal Differential Counting Flow Rate
Losses in different buffers and bead surfaces.

surements were performed with bead concentrations ranging from $6.5 \mu\text{L}^{-1}$ to $34 \mu\text{L}^{-1}$.⁵ The quotient of both measured concentration was determined after Eq. 4.13 and plotted in Fig. 18. Although, the optimal quotient value would have been 1 theoretically, an ideal

⁵ The raw data is shown in ??

overlap was found for a flow rate of $150 \mu\text{L min}^{-1}$. However, the difficulties in assembly and operation inhibited a further usage in experiments.

1.5. Surface Modification and Biofunctionalization of the Sensor Chip Substrate

1.5.1. Physisorption

Quantification in Plate Reader Trial with Neutravidin + Sensor (Esthis Versuch)

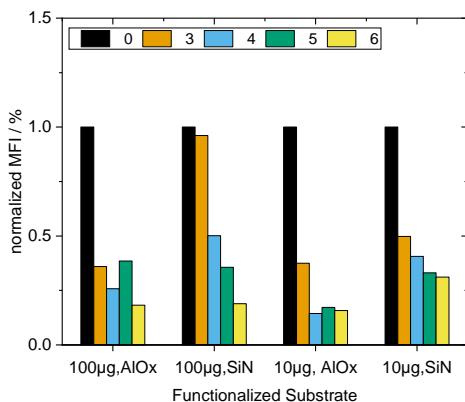


Figure 19: Surface Adsorption Stability of Neutravidin on Silicon nitride (Si_3N_4) and Aluminium oxide (Al_2Ox_3)
Blank with PBS and Blank substrate, corrected, then normalized, absolute protein per ~25 mm

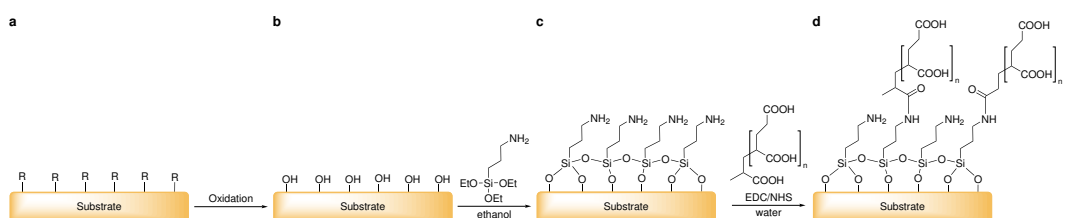


Figure 20: General process chain of chemical surface modification

Any substrate with various surface groups R (a) is oxidized to exhibit —OH (hydroxyl) groups.(b). Then a silane self-assembled monolayer (SAM) is attached (c) and subsequently modified by carbodiimide chemistry with poly(acrylic) acid (PAA). (d)

1.5.2. Covalent Attachment

Plasma-Based Approach

Water-Based Approach

Sonicate in Acetone and Water 5' 1:1 hydrochloric acid (HCl):Methanol sulfuric acid (H_2SO_4) Treat for 30 min in light boiling water

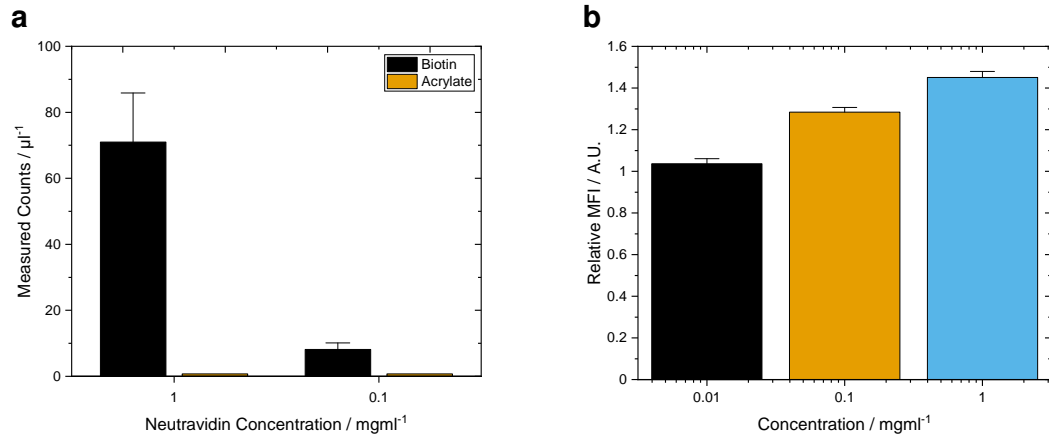


Figure 21: Neutravidin Titration Fluorescence and Bead Capture Assay
Relate count to area, then change MFI to counts $\mu\text{L}^{-1} \text{ mm}^{-2}$ (a) Serpentine (b) Glass

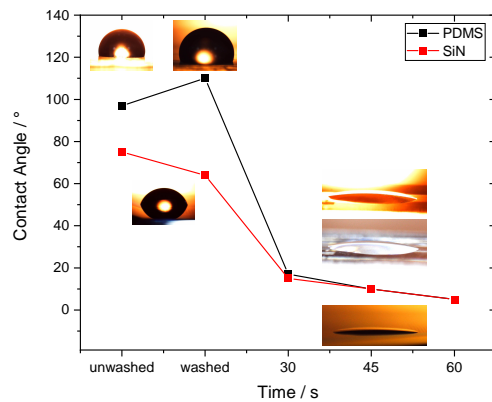


Figure 22: Hydrophobicity Analysis of poly(dimethylsiloxane) (PDMS) under Plasma Exposure
test123